Three-Dimensional Ultrasound Plaque Characterization

José Seabra, Jasjit S. Suri and J. Miguel Sanches

Abstract The chapter proposes a framework for extending the analysis of the atherosclerotic disease to a three-dimensional perspective. Different data acquisition systems, either based on a robotic arm setup or free-hand are proposed, in order to collect image sequences that completely describe the plaque anatomy. A 3D reconstruction method is proposed, comprising a Rayleigh based de-speckling approach and interpolation. As a consequence, 3D maps accounting for plaque echogenicity and texture, according to appropriate local Rayleigh estimators are obtained. Furthermore, the application of a segmentation approach which makes use of the Graph-cuts method, provides an efficient way to segment and locally identify unstable regions throughout the plaque. This information, complemented with a more accurate inspection of plaque morphology, may have an important clinical impact in disease diagnosis.

José Seabra and J. Miguel Sanches
Institute for Systems and Robotics and Department of Bioengineering from Instituto Superior Técnico / Technical University of Lisbon, Portugal e-mail: jseabra@ist.ist.utl.pt, jmrs@ist.utl.pt
Jasjit S. Suri
Biomedical Technologies Inc., Denver, CO, USA; Idaho State University (Aff.), ID, USA

1 Introduction

Atherosclerosis is a disease which generally affects large and medium-sized arteries and its most important feature is plaque formation due to progressive subendothelial accumulation of lipid, protein, and cholesterol esters in the blood vessel wall.

Several studies recognize that the degree of stenosis, obstruction to the blood flow, is an important physiological landmark of stroke but that other parameters, such as plaque echo-morphology and texture should also be considered for designing a plaque risk profile. Additionally, it has been observed that vulnerable plaques are usually associated with fibrous cap thinning and infiltration of inflammatory cells consequently leading to rupture. Other studies reported a positive correlation between the presence of fatty contents and hemorrhage with neurological symptoms, thus suggesting that that inflammatory activity potentially determines plaque instability. In Pedro *et al.* [1,2], the location and extension of these regions are identified as sensitive and relevant markers of stroke risk.

Numerous research groups conducted studies aiming at characterizing and identifying the main features of the symptomatic lesion [1,3–8]. Among these, the grey-scale median and P_{40} can be used to characterize the plaque from an echogenic viewpoint. However, the interpretation of these parameters values will fail to reveal possible unstable foci within the plaque, specially when plaques are heterogeneous or present significant hypoechogenic areas.

The risk assessment of plaque rupture through conventional 2D techniques is limited to a subjective selection of a representative image of plaque structure and it is hardly reproducible. An accurate diagnostic procedure based on 3D is known to be valuable but has not yet been adopted in clinical practice, mainly because such technology is not usually available in most medical facilities. Recently, less operator-dependent methods based on 3D US have been proposed from better assessment of plaque vulnerability [9,10]. These studies aim at quantifying the plaque volume, degree of stenosis [11], and the extension of surface ulceration [12].

The focus of this chapter is to assess the atherosclerotic disease on a 3D perspective providing better visualization of the lesion and characterization of potential risk. The carotid disease study in 3D is rooted on the reconstruction of 3D maps starting with 2D information extracted from noisy BUS images. To achieve the proposed objectives, different 3D image acquisition methods are explored and powerful methods for identifying vulnerable foci within the plaque volume are used.

2 Development of DAQ systems for 3D Ultrasound

Medical US has benefited from major advances in technology and is considered an indispensable imaging modality due to its flexibility and non-invasive character.

Currently, there are accurate methods to assess the disease severity based on CT [13] or MRI [14]. However their application is expensive, time consuming and

requires equipment which is not yet available and accessible in most clinical facilities. On the other hand, 2D ultrasound is widely available and provides real time data acquisition and visualization, so it has been so far the preferred technique in the diagnosis and monitoring of the disease.

Although all anatomy is 3D in form, the vast majority of US imaging is 2D. Most of the times, this technique provides sufficient information for diagnosis but there are clearly identifiable limitations, such as, non-ability to perform quantitative volume measurements or to obtain optimal 2D scan views of the anatomical ROI (*Region of Interest*). Consequently, 3D US is a logical solution to allow better, more complete and objective diagnostic results. In this imaging modality, the 2D US images are combined by a computer to form an objective 3D image of the anatomy and pathology. This data can be manipulated and measured in 3D both in real time or later offline. Moreover, unlike CT and MR imaging, in which 2D images are usually acquired at a slow rate as a stack of parallel slices, in a fixed orientation, US provides images at a high rate (15 to 60 s^{-1}) and in arbitrary orientations.

Most 3D US systems make use of a conventional transducer to obtain a sequence of images by sweeping the probe along the anatomical ROI, and differ only in acquisition and position sensing [9]. In this way, images can be acquired mechanically, free-handed with or without an optical or electromagnetic spatial locator and using 2D arrays. Some of these systems were validated in various clinical applications, such as obstetrics, cardiology and vascular imaging in order to increase the diagnosis confidence [15].

2.1 Robotic Arm Prototype

Depending on the organ or tissue to be scanned, it is necessary to apply different scanning strategies or protocols which comprise linear, rotatory and free-hand scanning, just to name the most common ones. Most imaging systems are not optimally adapted for such a wide range of applications. Hence, a 3D US prototype robotic system which can control, standardize and accurately perform the acquisition process is presented. This system may assist the operator in defining suitable scanning paths for each patient according to the ROI to be scanned. Different acquisition properties can be assigned in each examination, such as the duration and rate of image acquisition. Moreover, each image is assigned with its spatial information allowing to further perform following-up studies or to reconstruct and segment the tissues or organs scanned with higher degree of confidence.

Robotic systems can be regarded as an important diagnosis tool because they can simultaneously control and standardize the image acquisition process. Thus, they can be very suitable for quantifying and accurately monitor the development of cardiovascular diseases, namely, the progression of atheromatous plaques by scanning the carotid or coronary arteries [16]. In addition, the ability to remotely position the US probe with the robotic arm could also be used in telemedicine [17].

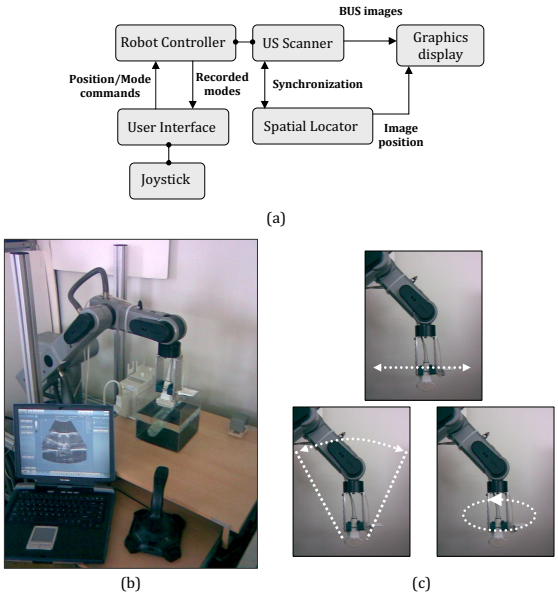

Fig. 1 Robotic Arm Prototype. (a) Block diagram of the system components. (b) Experimental setup. The robotic arm carries the probe and the position sensing receptor from the US scanner and the spatial locator, respectively. The workstation personal computer controls the movements of the robotic arm with the aid of a joystick. Images are tagged with their spatial location and showed on the screen. (c) Acquisition modes: linear (a), fan-like (b) and rotatory (c) scans.

Given this, a prototype medical robot is described which can easily be integrated with common ultrasound scanning equipment and provides clinicians with their regular scanning operations. The prototype robotic arm is schematically shown in Fig. 1(a) and comprises four main components. The first unit is the robotic arm (Scorbot-ER VII, Intelitek, USA) with six degrees of freedom which is operated from the robot controller. The second element is an US portable scanner (Echo Blaster 128, Telemed, LT), equipped with a linear array probe. This probe is attached to the tip of the robotic arm, together with an electromagnetic position sensing device (Fastrak, Polhemus, VT). The last component of the system is the computer workstation, which holds a joystick and the interface to control the medical robot and the US scanner.

A user-friendly graphical interface provides access and setting of the robotic arm controls and movements as well as visualization and tuning of acquisition results. The robotic arm is manipulated using a joystick which allows to move the US probe towards the ROI to be scanned. Moreover, the system features a *learning* mode which enables to store in memory a suitable scan path, and a *replay* mode to reproduce the manually taught path. This attribute of the robotic system is suitable to guarantee reproducible and personalized results since a scan path can be assigned

for each patient with controlled speed and accurate position information provided by the spatial locator.

The robot integrates several acquisition modes (see Fig. 1(c)), providing free-hand, linear, fan-like and rotatory scans. This should be flexible enough to allow image acquisition from different organs and tissues, where different scanning operations are needed. The system allows to capture BUS images at uniform spacing and user-defined sampling rate. These images are synchronized with the spatial locator and sent with their corresponding probe positions to the workstation for storage and further 3D reconstruction.

Fig. 1(b) shows the experimental robot setup for US image acquisition. A cross-section of a cylindrical latex-made phantom, which resembles a human vessel, was acquired and the result is shown on the computer screen.

This system provides accurate and standardize but at the same time flexible scanning of several organs and tissues. In particular, this can be a reasonable alternative to other 3D US imaging systems for accurately quantifying the progression of cardiovascular diseases.

2.2 Free-hand Ultrasound

A free-hand system can be also used to acquire BUS images for 3D Ultrasound. This strategy is more flexible than the robotic system presented above since it allows image acquisition with unconstrained movement. In general, a free-hand US image acquisition system consists of a sensor (attached to a probe) that is tracked by a device that calculates the sensor's position and orientation at any point in time. This information is used to compute the 3D coordinates of each pixel of the BUS images. In this context, there are four common technologies to track medical instruments, including mechanical, acoustical, electromagnetic, and optical.

The developed free-hand system is composed of an US duplex scanner (HDI 5000, Philips Medical Systems division, Bothell, WA, USA), depicted in Fig. 2(a) with a L12-5 scan probe (5 to 12 MHz broadband linear-array transducer), where a sensor from a tracking device was coupled as illustrated in Fig. 2(b). The designed system uses an electromagnetic sensing device (Fastrak, Polhemus, VT) providing storage of six degrees of freedom. The idea behind the electromagnetic system is to have a receiver placed on a probe that measures the induced electrical currents when moved within a magnetic field generated by a transmitter.

Generally, the tracking devices used for free-hand systems have the same operating mode. The device tracks the position and orientation of the sensor on the probe, not the BUS image plane itself. Hence, it is necessary to compute the transformation (rotation, translation and scaling) between the origin of the sensor mounted on the probe and the image plane itself. This problem can be tackled with the application of an adequate calibration method. Here, calibration was attained with a suitable software (Stradwin, Medical Imaging group at the Department of Engineering, University of Cambridge, UK) where all the experimental apparatus required is a flat

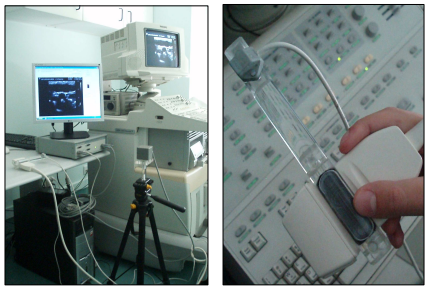

(a) (b)

Fig. 2 Free-hand 3D US. (a) Experimental setup, comprising a scanner, a spatial locator (b) and a computer interface for image visualization and acquisition.

plane immersed in a water tank. The flat plane could be as simple as the bottom of the water tank [18,19].

After calibration, every pixel in each 2D image is mapped in the 3D coordinate system of the tracking device to reconstruct a geometrically correct volume.

3 Methods

This section addresses the methods developed to study the atherosclerotic lesion from a 3D perspective. Hence, a description of the reconstruction procedure from sequences of BUS images acquired with the free-hand US system is described next. Moreover, a methodology for the local characterization (labeling) of hypoechogenic regions within the plaque volume is presented. The labeling procedure is based on Graph-cuts and it is expected to improve the characterization of plaques, by providing a more appropriate identification of unstable foci inside it.

3.1 Reconstruction

Two approaches are generally considered in organ and tissue reconstruction: surface and volume rendering. Surface rendering [12,20] can be used to extract the bifurcation walls of carotid arteries and quantify the degree of stenosis and plaque volume. A volume rendering approach [21] is often used to reconstruct a particular volume of interest from which echo-morphological or textural analysis can be performed. Here, a combination of the two approaches is used. First, volume renderings are obtained from sets of 2D BUS images of the carotid artery. The regions corresponding to atherosclerotic plaques are visually detected in several cross-sections taken from the obtained volume and then segmented using semi-automatic segmentation methods, e.g. active contours [22] guided by experienced physicians. Surface ren-

dering employs the interpolation of these contours providing a three-dimensional representation of the plaque. This procedure has been extensively described in [23].

It is recognized that BUS images are characterized by a speckle pattern which makes data visualization and interpretation a challenging task. The method used here to compute the morphology of the VOI (*Volume of Interest*) containing the carotid plaque is composed of two main steps: i) de-noising and ii) reconstruction.

The method used to accomplish de-noising is based on the approach described in [24] and can be summarized as follows. Let $Y = \{y_{i,j}\}$ be the original ultrasound image and $\Sigma = \{\sigma_{i,j}\}$ the de-speckled image to estimate. A Bayesian framework with the *Maximum a Posteriori* criterion (MAP) is adopted to deal with the ill poseness nature of this particular de-speckling problem. Hence, the de-speckled image is obtained by minimizing an energy function:

$$\hat{\Sigma} = \arg\min_{\Sigma} E(Y,\Sigma), \tag{1}$$

where $E(Y,\Sigma) = E_d(Y,\Sigma) + E_p(\Sigma)$. $E_d(Y,\Sigma)$, called *data fidelity* term, pushes the solution toward the data and $E_p(\Sigma)$, called *prior* term, regularizes the solution by introducing prior knowledge about Σ. The *data fidelity* term is the *log-likelihood* function, $E_d(Y,\Sigma) = -\log(p(Y|\Sigma))$ where $p(Y|\Sigma) = \prod_{i,j=1}^{N,M} p(y_{i,j}|\sigma_{i,j})$ and $p(y_{i,j}|\sigma_{i,j})$ is the Rayleigh probability density function [25]. The overall energy function obtained after considering the variable change $x = \log(\sigma^2)$ is:

$$E(Y,X) = \sum_{i,j} \left[\frac{y_{i,j}^2}{2} e^{-x_{i,j}} + x_{i,j} \right] + \alpha TV(\mathbf{X}) \tag{2}$$

where the prior term,

$$TV(X) = \sum_{i,j} \sqrt{(x_{i,j} - x_{i-1,j})^2 + (x_{i,j} - x_{i,j-1})^2}, \tag{3}$$

is the so called *Total Variation* (TV) of $\mathbf{X} = \{x_{i,j}\}$. An example to illustrate de application of the de-speckling algorithm is displayed in Fig. 3.

In the second step, these de-noised images are interpolated to estimate a 3D VOI containing the plaque. The 3D reconstruction of a VOI which completely contains the plaque aims at estimating a 3D field, $F = \{f_p\}$, from the de-noised images computed in the de-speckling step, $\Sigma^t = \{\sigma_{i,j}^t\}$, where t denotes the t^{th} image of the sequence of BUS images acquired with the presented 3D free-hand US system, and $p = (i,j,k)$ represents a node index in the 3D matrix, F. Two problems are naturally raised: (i) the node locations of F, f_p, and the locations of the pixels of Σ^t, $\sigma_{i,j}^t$, do not match, and (ii) some nodes may not be observed (missing data). These problems are tackled with an interpolation procedure described as follows.

Let us consider each voxel, f_p, as a cubic region centered at the location of the node μ_p, with dimensions $(\Theta_1, \Theta_2, \Theta_3)$ and the locations of the de-noised pixels $\sigma_{i,j}^t$ as $\tau_{i,j}^t$. Moreover, let $\Upsilon_p = \{\sigma_{r,l}^t : \tau_{r,l}^t \in S_{\Theta_1,\Theta_2,\Theta_3}(\mu_p)\}$ be the set of all pixels inside the neighborhood (voxel), $S_{\Theta_1,\Theta_2,\Theta_3}(\mu_p)$ of the node f_p displayed in Fig. 4.

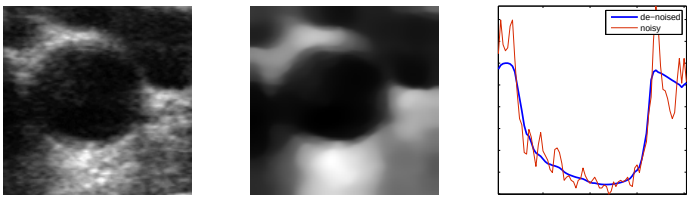

Fig. 3 De-speckling example (b) of an original ultrasound image (a). The algorithm clearly shows its edge-preserving nature (c).

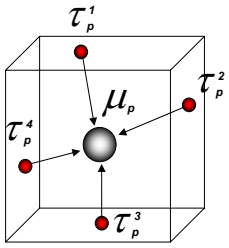

Fig. 4 Voxel representation associated with the node f_p (grey), located at μ_p, and several image pixels, at locations τ_p^r in its neighborhood (red).

In a first step, a 3D volume, $Z = \{z_p\}$ with the same dimensions of Σ is computed where each element, $z_p = \langle \Upsilon_p \rangle$, is the weighted mean of the set Υ_p where the weights are the normalized distances of the pixel locations to the center of the voxel, such that $z_p = (\sum_r \|\tau_r - \mu_r)\|\sigma_r)/(\sum_r \|\tau_r - \mu_p\|)$ where τ_r denotes the location of the r^{th} pixel within the set Υ_p. Therefore, each element of Z contains the average intensity of the pixels within the voxel. However, some elements of Z may be undefined when there are no observations (pixels) inside the voxel. In this case an interpolation is needed. This missing data problem may be solved by minimizing the following energy function:

$$E(F,Z) = \sum_p [n_p(f_p - z_p)^2 + g_p^2], \tag{4}$$

where $g_p = \sqrt{(f_{i,j,k} - f_{i-1,j,k})^2 + (f_{i,j,k} - fi,j-1,k)^2 + (f_{i,j,k} - f_{i,j,k-1})^2}$ is the gradient magnitude of F at the voxel p and n_p is the number of observations (pixels) associated with the voxel p. The minimization of (4) can be iteratively solved by optimizing with respect to one unknown at a time, which leads to the following recursion:

$$f_p^t = \beta(n_p) z_p + (1 - \beta(n_p)) \overline{f_p^{t-1}}, \tag{5}$$

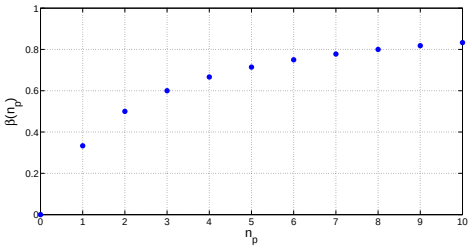

Fig. 5 Regularization parameter function depending on the number of observed pixels.

where $()^t$ denotes the iteration t, $\overline{f_p^{t-1}}$ corresponds to the mean value of the neighbors of f_p computed in the iteration $t-1$, n_p is the number of pixels inside the voxel and

$$\beta(n_p)) = \frac{n_p}{n_p + N_v} \tag{6}$$

is a regularization parameter function with $N_v = 6$, whose behavior is illustrated in Fig. 5. The equation expressed in (5) reveals the underlying interpolation mechanism performed during the minimization of the energy function (4). Each new estimate of F, F^t, is dependent of the previous estimate, F^{t-1}, and of the field of the mean pixel intensities, Z, computed in the previous step. As large is the number of pixels, n_p, associated with a particular voxel, the closer to the unity is the parameter β, meaning that, in the limit, $f_p^t \approx z_p$. Conversely, a small number of observed pixels leads to small values of β, $\overline{f_p^{t-1}}$, meaning that new estimates of f_p^t are computed part from z_p and part from the neighbors, $\overline{f_p^{t-1}}$, estimated in the previous iteration. In the limit, when no observations are available, $\beta = 0$, and the new estimate is $f_p^t = \overline{f_p^{t-1}}$, that is, it corresponds to the mean intensity of its neighbors. To summarize this method is based on the following concept: when a large number of pixels are available for a given voxel its value is mainly computed from Z, whereas when the number of observations is small or even zero the estimate is obtained from the voxel neighborhood values.

The volume field F, originated from the set of de-speckled images, describes the value of the Rayleigh parameter across the VOI enclosing the carotid plaque and it may be used to compute local intensity and textural indicators which characterize the different components and tissues of the plaque. Volume reconstruction of the plaque interior provides an overall characterization of its composition which is in most cases mentally built up by the clinician.

Traditionally, plaque characterization is based on statistics computed from the observed noisy pixels. Here, instead of computing these indicators from the noisy data, the characterization is based on theoretical statistical estimators depending on F, and consequently on the plaque acoustical properties encoded in the Rayleigh distribution.

Given this, with the purpose of assessing the local echo-morphology of the 3D reconstructed plaque, the median and the P_{40} are computed, since these indicators already demonstrated to be useful for tissue characterization. These statistics, derived from the Rayleigh distribution [26], are given by:

$$\begin{cases} f_v(p) = f_p\sqrt{\log(4)} \\ f_{P_{40}}(p) = 1 - \exp\left(-\frac{40^2}{2f_p^2}\right). \end{cases} \tag{7}$$

Consequently, two different maps, F_v and F_{P40} are computed containing the values of the mentioned estimators at each location $p = (i, j, k)$. By averaging the elements of these 3D matrices, a rough (global) characterization of the plaque echomorphology can be performed.

3.2 Local hypoechogenic region labeling with Graph-cuts

As mentioned before, the global characterization of carotid plaques, despite its unquestionable usefulness, may not be accurate for an objective assessment of plaque vulnerability, especially in cases where the plaque is significantly heterogeneous or is plagued by artifacts.

In this section a local-based labeling approach was developed. The goal is to use statistical estimators (7) to assess the risk of plaque rupture on a localwise basis. This method is expected to identify regions of the plaque whose hypoechogenicity information point towards potential foci of vulnerability. Plaque classification at each location $p = (i, j, k)$ can be made by comparing the statistics derived in (7) with a threshold, defined by the clinician. Considering the median and $P40$, conventional reference values are 32 and 43, respectively [1,27]. This is done for every voxel, resulting in 3D maps of labels ascribed for each one of the clinical indicators. This thresholding algorithm is simple and fast but it does not take into account spatial correlation between neighboring nodes because the process is performed on a voxel-by-voxel basis.

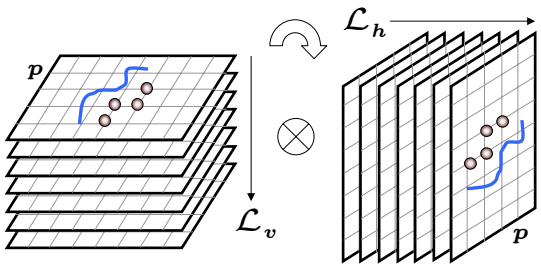

Fig. 6 Labeling procedure performed on a plane by plane basis, providing $\mathscr{L}_v$ and $\mathscr{L}_v$.

Here, a more sophisticated and accurate method is used where the labeling procedure considers the intensity value of the statistical function at location p and also the values of its neighboring nodes. The goal is to introduce spatial correlation to reduce the misclassification rate by assuming that the plaque is piecewise homogeneous, that is, composed of homogeneous regions separated by abrupt transitions. This assumption is acceptable from an anatomical perspective and is usually adopted for de-noising and de-blurring in medical imaging.

Let f_p be the estimated value of F at the p^{th} node. The labeled maps, $\mathscr{L}_\tau$ with $\tau = \{v, P_{40}\}$, are performed on a plane-by-plane basis, i.e. each plane is labeled independently of the others. The segmentation is binary, which means $\mathscr{L}(p) \in \{0,1\}$ where $\mathscr{L}(p)$ is the p^{th} node of the labeled volume. The labeling procedure of the whole volume is performed in three steps, as depicted in Fig. 6: (i) all stacked planes along the vertical direction are independently labeled, (ii) all stacked planes along the horizontal direction are independently labeled, and (iii) both volumes obtained in the previous steps, $\mathscr{L}_v(p)$ and $\mathscr{L}_h(p)$, are fused by making $\mathscr{L}(p) = \mathscr{L}_v(p) \otimes \mathscr{L}_h(p)$ where $\otimes$ denotes the boolean product.

The labeling process of each plane is performed by solving the following optimization problem:

$$\mathscr{L}_\tau = \arg\min_{\mathscr{L}} E(F_\tau, \mathscr{L}), \tag{8}$$

where the energy function is given by:

$$\begin{aligned} E_\tau(F_\tau, \mathscr{L}) = \sum_p (\lambda_\tau - f_p)(2\mathscr{L}(p) - 1) - 1 + \\ \theta \sum_p \left(\frac{V(\mathscr{L}(p), \mathscr{L}(p_v)) + V(\mathscr{L}(p), \mathscr{L}(p_h))}{\tilde{g}_p} \right), \end{aligned} \tag{9}$$

where λ_τ is the threshold associated with the indicator τ, θ is a parameter to tune the strength of smoothness, $\tilde{g_p}$ is the normalized gradient at location p, and p_v and p_h are the locations of the causal vertical and horizontal neighbors of the p^{th} node. In addition, $V(l_1, l_2)$ is a penalization function defined as follows:

$$V(l_1, l_2) = \begin{cases} 0 & l_1 = l_2 \\ 1 & l_1 \neq l_2. \end{cases} \tag{10}$$

The energy function (9) is composed of two terms: the first called *data term* and the second designated as *regularization term*. The first forces the classification to be $\mathscr{L}(p) = 1$ when $f_p \geq \lambda_\tau$ because this leads to a decrease in the term $(\lambda_\tau - f_p)(2\mathscr{L}(p) - 1)$ when compared to the alternative classification, $\mathscr{L}(k) = 0$. The opposite occurs if $f_p < \lambda_\tau$. The second term forces the uniformity of the solution because the cost associated with uniform labels is smaller than with non-uniform ones (10). In order to preserve the transitions the terms are divided by the normalized gradient magnitude of f_p, $\tilde{g}_p$. Therefore, when the gradient magnitude increases the regularization strength is reduced at that particular location.

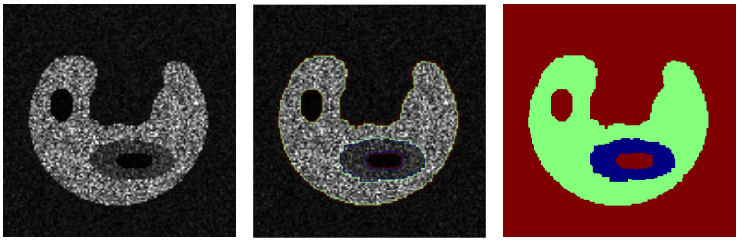

Fig. 7 Illustration of labeling based on Graph-cuts using a synthetic plaque corrupted with Rayleigh noise. Different classes (regions) are correctly labeled.

The minimization of (9) formulated in (8) is a huge optimization task performed in the Ω^{NM} high dimensional space where $\Omega = \{0,1\}$ is the set of labels and N and M are the dimensions of the image. In [28] it is shown that several energy minimization problems in high dimensional discrete spaces can be efficiently solved by use of *Graph-cuts* [29]. Opportunely, the energy function given in (9) belongs to this class of problems, for which the authors have designed a very fast and efficient algorithm to compute the global minimum. For example, a 200×300 pixel image is processed in 0.2 seconds in an Intel Core2 CPU at 1.83GHz with 2GB RAM, which shows the efficiency and the short processing time of the method.

4 Experimental Results

The first result aims at investigating the adequacy of the labeling procedure to detect piecewise smooth regions in synthetic ultrasound data. For this purpose, it is used a synthetic BUS image (Fig. 7(a)) created from a plaque phantom presenting two hypoechogenic regions ($f_p = 20$), one low echogenic region ($f_p = 35$) and the echogenic foreground ($f_p = 50$). The background is assumed to be hypoechogenic ($f_p = 20$). The synthetic image is corrupted with Rayleigh noise using MatLab software. Here, the number of classes (regions with homogeneous echogenicity) to detect is set to 3 and the *data term* is simply the image intensities. This simple example provides an illustration of how the Graph-cuts algorithm is able to correctly label the different portions of the synthetic BUS image (Fig. 7(b)-Fig. 7(c)).

Furthermore, the performance of 3D reconstruction and labeling was evaluated with a set of 100 synthetic images created as in the aforementioned example. This image set defines a 3D VOI, as illustrated in Fig. 8(a). Each image is corrupted with noise and interpolated, thus creating the noisy VOI shown in Fig. 8(b). After de-speckling each image and performing 3D reconstruction, the obtained result is shown in Fig. 8(c). Clearly, speckle has been significantly suppressed, providing a clearer VOI where the plaque is can be easily identified. Moreover, the application of de-speckling followed by 3D reconstruction eases the task of 3D labeling, whose

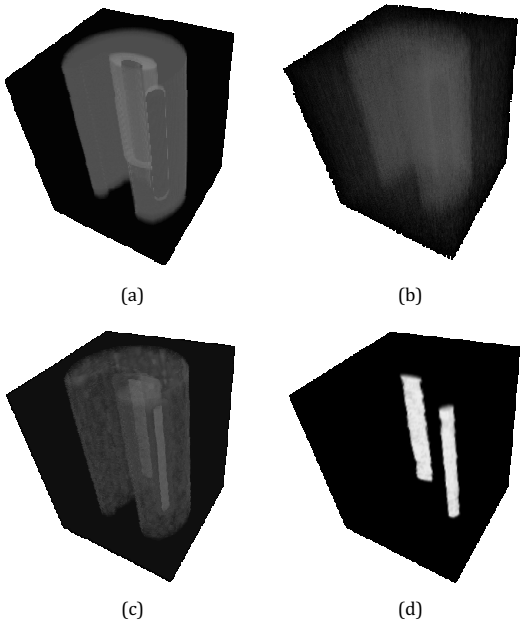

Fig. 8 3D reconstruction and labeling using Graph-cuts from a synthetic image set.

results are shown in Fig. 8(d). In fact, the hypoechogenic regions, hypothetically considered as defining *foci* of plaque instability, are correctly identified by use of the labeling procedure based on Graph-cuts, where $f_\lambda = 20$ in (9).

The effectiveness of the labeling procedure based on Graph-cuts for local identification of unstable sites inside the plaque is evaluated in real ultrasound data. Three carotid plaques were reconstructed following the previously proposed method and then locally characterized using the median and $P40$ estimators derived from each reconstructed VOI, f_p, that is, $f_v(p)$ and $f_{P40}(p)$. As mentioned, the analysis of plaque echo-morphology, in particular the GSM (median) and $P40$ determines whether (or not) a plaque is stable by using consensual thresholds given in the literature [1,2,30], which in this context corresponds to $f_v(p) < 32$ and $f_{P40}(p) > 43$. This binary classification, based on a thresholding procedure, is very simple and can lead to non realistic clinical results as physicians would expect to identify clusters (regions) of vulnerability across the carotid plaques, where isolated or dispersed pixels (outliers) are not expected to occur. Hence, the application of a strategy such as that based on Graph-cuts can be suitable for this particular labeling problem since it favors clustering. The labeling procedure based on Graph-cuts is applied by considering the 3D maps of the median and P_{40}, $f_v(p)$ and $f_{P_{40}}(p)$, and the corresponding reference "cut-offs", $f_\lambda = 32$ and $f_\lambda = 43$, in (9).

Fig. 9 displays the labeling of potentially dangerous sites inside the plaque using two labeling strategies, where the first is based on thresholding and the second on

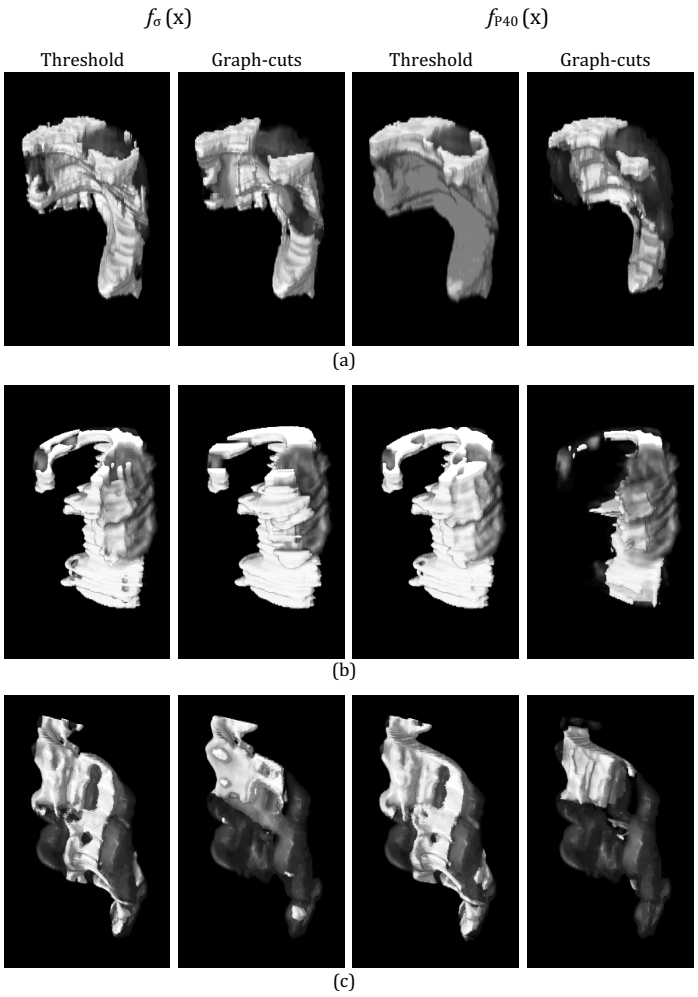

Fig. 9 Comparison of labeling strategies based on simple threshold and Graph-cuts computed from the median and *P*40 3D maps of three reconstructed plaques.

Graph-cuts. It is observed that the use of Graph-cuts allows to better discriminate the hypoechogenic sites across the carotid plaques. Volumes labeled with Graph-cuts appear less noisier than when the threshold method is used. This suggests that the use of Graph-cuts may improve the characterization of carotid plaques, namely by providing a more appropriate identification and definition of unstable regions across the plaque. This result can be clinically meaningful since as reported in [1] the degree of extension of these unstable regions and their location throughout the plaque should be considered and used as markers of risk of plaque rupture and thus of stroke risk.

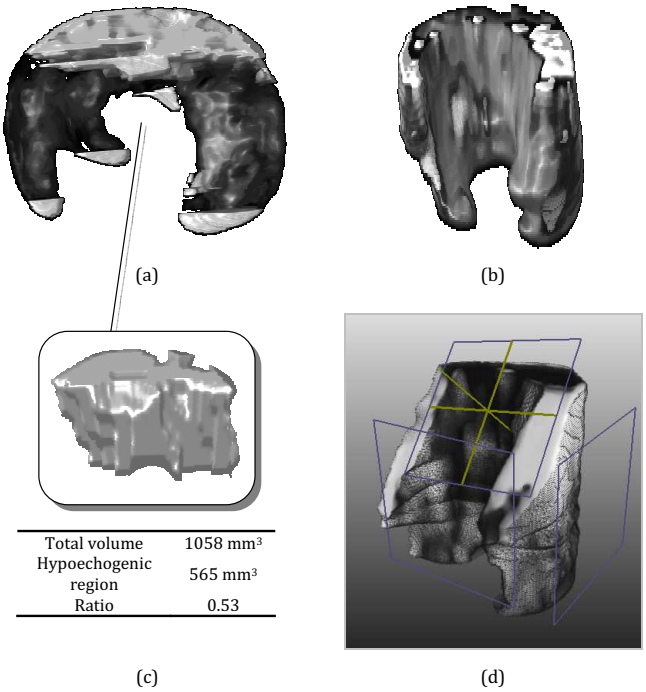

Fig. 10 Potential application of the algorithm: (a) Identification of hypoechogenic sites, using the local median parameter; (b) Inspection and quantification of a representative vulnerable region detected inside the plaque; (c) Gray-scale mapping of plaque texture, using the local standard deviation parameter;

Fig. 10 depicts a potential application of the reconstruction and labeling algorithms in the scope of 3D plaque analysis with ultrasound. First, regions of hypoechogenicity are identified by use of the local median estimator, $f_v(p)$), and the Graph-cuts labeling strategy (Fig. 10(a)). Fig. 10(b) illustrates a potential application of the characterization algorithm based on the inspection of a region which was identified by the algorithm as being more vulnerable. This region can be extracted, its location inside the plaque can be tracked and its volume can be computed to assess the ratio of its occupation related to the whole plaque.

Moreover, Fig. 10(c) shows results of plaque texture, based on the standard deviation estimator which is computed as $f_\sigma(p) = \frac{4-\pi}{2} f_p^2$ [30], providing a gray-scaled indicator of plaque heterogeneity. Regions resulting from the combination of the previous results are thought to be the most important foci of plaque rupture.

The 3D approach provides the visualization of an unlimited number of cross-sectional cuts of the plaque which naturally eases the analysis of its echo-morphology contents and surface regularity (Fig. 10(d)).

5 Conclusions

The assessment of plaque morphology, echogenicity and texture is considered to be critical for an accurate diagnosis of atherosclerotic disease. 2D ultrasound has so far been the preferred imaging technique because it is non-invasive, inexpensive and portable. This chapter proposes an extension to the traditional characterization of plaques using a 3D approach. This strategy provides a more complete and objective description of lesion severity because it considers all the information enclosed in the plaque anatomical volume without depending on a subjective selection of a particular image for diagnosis.

Two distinct data acquisition systems developed for 3D ultrasound, either robotic arm and free-hand based, are proposed to obtain a set of cutting planes of the carotid plaque acquired at a high sampling rate and in virtually any arbitrary orientation.

Moreover, the VOI containing the plaque is obtained in two steps, where the first uses the proposed de-speckling algorithm applied to each image of the acquired data sequence and the second considers a reconstruction step. The application of such procedure provides a description of plaque echogenicity and texture in terms of 3D maps of local estimators obtained from the Rayleigh distribution. Consequently, plaque analysis can be performed on a global sense, where the average values of Rayleigh descriptors are computed, or on a local basis.

The latter approach is crucial from a clinical perspective because it potentially allows the identification of sources of plaque rupture. To tackle this problem, a labeling method is introduced using an efficient method based on Graph-cuts. Such labeling procedure improves the segmentation of potential foci of instability across the plaque because it is robust to the presence of noise and favors clustering. Results of local labeling using synthetic and real data show that this strategy outperforms the method based on simple thresholding.

Hence, an entire 3D ultrasound-based framework was introduced, from data acquisition, reconstruction to its analysis, providing a more complete and objective characterization of carotid plaques. This study presents encouraging and meaningful results in terms of plaque inspection, quantification and local characterization of plaque echo-morphology.

References

1. L.M. Pedro, J.F. Fernandes, M.M. Pedro, I. Gonçalves, and N.V. Dias. Ultrasonographic risk score of carotid plaques. *European Journal of Vascular and Endovascular Surgery*, 24:492–498, December 2002.
2. L.M. Pedro. *Uma janela para a aterosclerose. A ultrassonografia de alta definição no estudo da parede arterial*. PhD thesis, Faculdade de Medicina de Lisboa, 2003.
3. C.I. Christodoulou, C.S. Pattichis, M. Pantziaris, and A. Nicolaides. Texture-based classification of atherosclerotic carotid plaques. *IEEE Transactions on Medical Imaging*, 22(7), 2003.
4. S. Mougiakakou, S. Golemati, I. Gousias, A. N. Nicolaides, and K. S. Nikita. Computer-aided Diagnosis of Carotid Atherosclerosis based on Ultrasound Image Statistics, Laws' texture and Neural networks. *Ultrasound in Medicine & Biology*, 33(1):26–36, Jan 2007.
5. E. Kyriacou et al. Classification of Atherosclerotic Carotid Plaques using Morphological Analysis on Ultrasound Images. *Applied Intelligence*, 30(1):3–23, Feb 2009.
6. T. Elatrozy, A. Nicolaides, T. Tegos, and M. Griffin. The objective characterization of ultrasonic carotid plaque features. *Eur J Vasc Endovasc Surg*, 16:223–230, 1998.
7. L.M. Pedro, M.M. Pedro, I. Goncalves, T.F. Carneiro, and C. Balsinha. Computer-assisted carotid plaque analysis: characteristics of plaques associated with cerebrovascular symptoms and cerebral infarction. *Eur J Vasc Endovasc Surg*, 19(2):118–123, Feb 2000.
8. A.N. Nicolaides, S.K. Kakkos, M. Griffin, M. Sabetai, S. Dhanjil, et al. Severity of Asymptomatic Carotid Stenosis and Risk of Ipsilateral Hemispheric Ischaemic Events: Results from the ACSRS Study. *European Journal of Vascular & Endovascular Surgery*, 30(3):275–284, 2005.
9. A. Fenster, D.B. Downey, and H.N. Cardinal. Three-dimensional ultrasound imaging. *Phys Med Biol*, 46(5):67–99, May 2001.
10. A. Landry, J.D. Spence, and A. Fenster. Measurement of Carotid Plaque Volume by 3-Dimensional Ultrasound. *Stroke*, 35(4):864–869, 2004.
11. C.D. Ainsworth, C.C. Blake, A. Tamayo, V. Beletsky, and A. Fenster. 3D ultrasound measurement of change in carotid plaque volume: a tool for rapid evaluation of new therapies. *Stroke*, 36(9):1904–1909, 2005.
12. U. Schminke, L. Motsch, L. Hilker, and C. Kessler. Three-dimensional ultrasound observation of carotid artery plaque ulceration. *Stroke*, 31(7):1651–1655, 2000.
13. M. Wintermark, S.S. Jawadi, J.H. Rapp, T. Tihan, E. Tong, D.V. Glidden, S. Abedin, S. Schaeffer, G. Acevedo-Bolton, B. Boudignon, B. Orwoll, X. Pan, and D. Saloner. High-Resolution CT Imaging of Carotid Artery Atherosclerotic Plaques. *AJNR Am J Neuroradiol*, 29(5):875–882, 2008.
14. Tobias Saam, Chun Yuan, Baocheng Chu, Norihide Takaya, Hunter Underhill, Jianming Cai, Nam Tran, Nayak L. Polissar, Blazej Neradilek, Gail P. Jarvik, Carol Isaac, Gwenn A. Garden, Kenneth R. Maravilla, Beverly Hashimoto, and Thomas S. Hatsukami. Predictors of carotid atherosclerotic plaque progression as measured by noninvasive magnetic resonance imaging. *Atherosclerosis*, 194(2), October 2007.
15. T. R. Nelson. Three-dimensional imaging. *Ultrasound in Medicine & Biology*, 26 Suppl 1:35–38, May 2000.
16. F. Pierrot et al. Hippocrate: a safe robot arm for medical applications with force feedback. *Medical Image Analysis*, 3(3):285–300, Sep 1999.
17. J. Sublett, B. Dempsey, and A. Weaver. Design and implementation of a digital teleultrasound system for real-time remote diagnosis. In *Symposium on Computer-Based Medical Systems*, pages 292–298, 1995.
18. R.W. Prager, R.N. Rohling, A.H. Gee, and L. Berman. Rapid calibration for 3-D freehand ultrasound. *Ultrasound in Medicine & Biology*, 24(6):855–869, 1998.
19. P. Hsu, R. W. Prager, A. H. Gee, and G. M. Treece. Rapid, easy and reliable calibration for freehand 3d ultrasound. *Ultrasound in Medicine & Biology*, 32(6):823–835, 2006.
20. S. Meairs and M. Hennerici. Four-dimensional ultrasonographic characterization of plaque surface motion in patients with symptomatic and asymptomatic carotid artery stenosis. *Stroke*, 30(9):1807–1813, 1999.

21. E. Bullitt and S.R. Aylward. Volume rendering of segmented image objects. *IEEE Transactions on Medical Imaging*, 21(8):998–1002, 2002.
22. C. Xu and J.L. Prince. Snakes, shapes, and gradient vector flow. *IEEE Transactions on Image Processing*, 7(3), Mar 1998.
23. J.C. Seabra, L.M. Pedro, J. Fernandes e Fernandes, and J.M. Sanches. A 3D Ultrasound-Based Framework to Characterize the Echo-Morphology of Carotid Plaques. *IEEE Transactions on Biomedical Engineering*, 56(5):1442–1453, May 2009.
24. J. Seabra, J. Xavier, and J. Sanches. Convex ultrasound image reconstruction with log-euclidean priors. In *Proceedings of IEEE International Conference on Engineering in Medicine and Biology*, pages 435–438, Vancouver, Canada, Aug 2008. IEEE Engineering in Medicine and Biology Society.
25. T. Eltoft. Modeling the amplitude statistics of ultrasonic images. *IEEE Transactions on Medical Imaging*, 25(2):229–240, Feb 2006. Comparative Study.
26. M. Abramowitz and I.A. Stegun. *Handbook of Mathematical Functions with Formulas, Graphs, and Mathematical Tables*. Dover, New York, ninth dover printing, tenth gpo printing edition, 1964.
27. N.M. El-Barghouty, T. Levine, S. Ladva, A. Flanagan, and A. Nicolaides. Histological verification of computerised carotid plaque characterisation. *Eur J Vasc Endovasc Surg.*, 11(4):414–416, 1996.
28. V. Kolmogorov and R. Zabih. What energy functions can be minimizedvia graph cuts? *IEEE Trans. Pattern Anal. Mach. Intell.*, 26(2):147–159, 2004.
29. Y. Boykov, O. Veksler, and R. Zabih. Fast approximate energy minimization via graph cuts. *IEEE Trans. Pattern Anal. Mach. Intell.*, 23(11):1222–1239, 2001.
30. L.V. Baroncini, A.P. Filho, L. Junior, A.R. Martins, and S.G. Ramos. Ultrasonic tissue characterization of vulnerable carotid plaque: correlation between videodensitometric method and histological examination. *Cardiovascular Ultrasound*, 4:32, 2006. Comparative Study.